GEOPHYSICS, VOL. 80, NO. 4 (JULY-AUGUST 2015); P. T147–T160, 13 FIGS., 1 TABLE.
10.1190/GEO2014-0563.1

Comparison of two algorithms for isotropic elastic P and S vector decomposition

Wenlong Wang[1], George A. McMechan[1], and Qunshan Zhang[2]

ABSTRACT

P- and S-wavefield separation is necessary to extract PP and PS images from prestack elastic reverse time migrations. Unlike traditional separation methods that use curl and divergence operators, which do not preserve the wavefield vector component information, we did P and S vector decomposition, which preserves the same vector components that exist in the input elastic wavefield. The amplitude and phase information was automatically preserved, so no amplitude or phase corrections were required. We considered two methods to realize P and S vector decomposition: selective attenuation and decoupled propagation. Selective attenuation uses viscoelastic extrapolation, in which the Q-values are used as processing parameters, to remove either the P-waves or the S-waves. Decoupled propagation rewrites the stress and particle velocity formulation of the elastic equations into separate P- and S-wave components. In both methods, the decomposition is realized during the extrapolation of an elastic wavefield. These algorithms could also perform P and S decomposition in x-t gather data by extrapolating the data downward from the receivers, during which the decomposition is performed, and then back upward to record the decomposed P- and S-waves at the receivers. Comparisons of the two methods in terms of efficiency, accuracy, and memory showed that both could separate P- and S-waves in the vector domain. The decoupled propagation is preferable in terms of speed and memory cost, but was applicable only to elastic propagation.

INTRODUCTION

Separation of P- and S-waves is a necessary part of elastic migrations. In multicomponent seismic data, P- and S-wave modes exist in each particle-velocity component, so using a component-by-component crosscorrelation imaging condition of unseparated source and receiver wavefields will lead to crosstalk artifacts between different wave modes during migration.

Many methods have been proposed to solve the separation problem. Helmholtz decomposition is widely used to separate the elastic wavefield (Morse and Feshbach, 1953; Clayton, 1981; Mora, 1987). Sun (1999) and Sun and McMechan (2001) perform elastic extrapolation and use divergence and curl operators to separate the P and S wavefields near the surface, followed by two acoustic reverse time migrations (RTMs), one for the P-P reflection and one for the converted P-S reflection. Dellinger and Etgen (1990) propose divergence-like and curl-like operators in the wavenumber domain based on Helmholtz theory, and they use the Christoffel equation to realize the decomposition in anisotropic homogeneous elastic media. Yan and Sava (2008) transform the separation operator from the wavenumber domain to the space domain, and they formulate a filter to separate wavefields in heterogeneous transversely isotropic media with a vertical symmetry axis (VTI media).

The above separation schemes all involve using divergence and curl, or similar, operators on the propagating elastic wavefields, which generate a scalar wavefield (divergence) and a vector wavefield (curl) with a different physical meaning from the input elastic wavefield. Thus, the amplitude and phase are changed, and much effort needs to be spent on corrections to obtain well-focused, true-amplitude images from prestack elastic RTM. To avoid this problem, Zhang and McMechan (2010) extend Dellinger and Etgen's (1990) theory to separate wavefields in VTI media into P- and S-particle components (vector decomposition), which is desirable, but computationally expensive because of the forward and inverse

Manuscript received by the Editor 30 November 2014; revised manuscript received 11 March 2015; published online 10 June 2015.
[1]The University of Texas at Dallas, Center for Lithospheric Studies, Richardson, Texas, USA. E-mail: wxw120130@utdallas.edu; mcmec@utdallas.edu.
[2]Repsol Services Company, The Woodlands, Texas, USA. E-mail: qunshan.zhang@repsol.com.

fast Fourier transforms (FFTs) at each time step. Cheng and Fomel (2014) use a low-rank approximation to reduce the number of FFT operations per time step. However, for practical applications in isotropic media, we seek simpler and less expensive P and S decomposition algorithms.

In this paper, two affordable, yet accurate, algorithms that do not use FFTs are analyzed and compared; both methods decompose the vector P- and S-waves in an isotropic elastic wavefield during wavefield extrapolation. The first algorithm is selective attenuation, in which attenuation is used as a tool to decompose the wavefields; the viscoelastic extrapolation is implemented with memory variables (Carcione et al., 1988a). The P and S decomposition is achieved during the extrapolation by applying strong attenuation to either P- or S-waves while preserving the other wave mode.

The second method is decoupled propagation. Ma and Zhu (2003) solve the decoupled isotropic elastic wave equations during extrapolation in a pseudospectral formulation. Zhang et al. (2007) use a decoupled 2D staggered-grid stress and particle-velocity formulation to decompose the elastic wavefield. Xiao and Leaney (2010) use different, but equivalent, equations to do wavefield decomposition for elastic interferometric RTM of VSP data. Both decomposition methods are embedded in wavefield extrapolation, and the output P- and S-wavefields are the same vector components as the input wavefields. The advantages of vector-domain elastic wavefield decomposition suggest direct applications in elastic prestack RTM, and the relation between the decomposed elastic wavefield vectors and propagation directions can be applied in generating PP and PS angle-domain common-image gathers (ADCIGs). However, these are beyond the scope of this paper and will be discussed elsewhere.

This paper is organized as follows: First, the methodologies of selective attenuation and decoupled propagation methods are introduced, followed by tests on synthetic data to show the decomposition results. Then, we present a systematic comparison of the two methods in terms of accuracy, speed, memory usage, and numerical stability criteria. Finally, inspired by the work of Sun (1999), we decompose x-t multicomponent data into P- and S-seismograms using decoupled propagation.

METHODOLOGY

To demonstrate the necessity to do wavefield decomposition, we use divergence ($\nabla\cdot$) and curl ($\nabla\times$) operators (Dellinger and Etgen, 1990) as the benchmark method to separate the wavefield as

$$\theta = \nabla \cdot \mathbf{u} \tag{1}$$

and

$$\boldsymbol{\varphi} = \nabla \times \mathbf{u}, \tag{2}$$

where $\mathbf{u}$ is the displacement of the elastic wavefield and θ and $\boldsymbol{\varphi}$ represent the separated P- and S-waves (Aki and Richards, 1980). Particle velocity can be substituted for displacement; θ and $\boldsymbol{\varphi}$ are dimensionless and have no physical interpretation. However simple and elegant the method might be, the divergence and curl operators do not preserve the features of the input elastic wavefield. In equation 1, θ is a scalar, and in equation 2, $\boldsymbol{\varphi}$ is a vector that is locally perpendicular to the S-wave polarization. The spatial derivatives in $\nabla\cdot$ and $\nabla\times$ produce a 90° phase shift in the wavelet, thus making the amplitude and phase produced by any imaging condition unphysical and migrations difficult to implement and interpret, especially for P-S converted reflections. To overcome this problem, and to obtain accurate migration images, corrections to the amplitude and phase need to be made. A Hilbert transform can be used to correct the phase information (Sun et al., 2001), and amplitudes need to be calibrated with knowledge of P- and S-wave velocities (Sun et al., 2011; Nguyen and McMechan, 2015) using

$$\frac{|\mathbf{u}_\mathrm{P}|}{|\mathbf{u}_\mathrm{S}|} = \frac{\theta}{|\boldsymbol{\varphi}|}\frac{V_\mathrm{P}}{V_\mathrm{S}}, \tag{3}$$

where $|\mathbf{u}_\mathrm{P}|$ and $|\mathbf{u}_\mathrm{S}|$ are the magnitudes of the displacement vectors of the P- and S-waves and V_P and V_S are the P- and S-wave propagation velocities, respectively.

The corrections for divergence and curl involve additional computation and may introduce artifacts. A better solution is to decompose the elastic wavefield while preserving the original particle components that are present in the input elastic data, so the amplitude and phase are naturally accurate. In the following two subsections, two methods for wavefield-decomposition are introduced, investigated, and illustrated.

Selective attenuation

The basic idea of selective attenuation is to modify the viscoelastic extrapolator to attenuate one wave mode during the wavefield extrapolation while preserving the other. Viscoelastic extrapolations have previously been used to simulate the anelastic phenomena of the real earth. The theory of linear viscoelasticity is based on the superposition of relaxation mechanisms (Liu et al., 1976; Emmerich and Korn, 1987). The standard linear solid model implements the process of attenuation (Zener, 1948). In this formulation, the moduli become functions of time and frequency:

$$\boldsymbol{\sigma} = \boldsymbol{\Psi} * \dot{\boldsymbol{\epsilon}}, \tag{4}$$

where $\boldsymbol{\sigma}$ is the stress tensor, $\boldsymbol{\epsilon}$ is the strain tensor, $\boldsymbol{\Psi}$ is the modulus, and the dot denotes a time derivative: $\boldsymbol{\sigma}$, $\boldsymbol{\epsilon}$, and $\boldsymbol{\Psi}$ are all time dependent. Dissipation of energy occurs when stress and displacement are out-of-phase (e.g., Guéguen and Palciauskas, 1994). Carcione et al. (1988a, 1988b) replace the convolution operation in equation 4 by using memory variables. Memory variables allow the computation of synthetic wavefields for models with arbitrary spatial distributions of quality factors. Xu and McMechan (1995) use composite memory variables to reduce the number of memory variables to be stored.

The quality factor Q characterizes the attenuation of waves in earth materials, and it is a measure of the number of wavelengths through which a wave must propagate in a material for its amplitude to decrease by $1/e$ (e.g., Robertsson et al., 1994). Earth materials have been shown to have nearly constant quality factors (Q-values), over the exploration seismic frequency range (McDonal et al., 1958; Bourbie et al., 1987). Usually, more than one of the relaxation mechanisms are combined to construct a desired Q behavior as a function of frequency. However, this is not necessary for the purpose of wavefield decomposition, in which Q is treated as a processing parameter; thus, having only one relaxation mechanism is

sufficient, and the computations are simplified. Figure 1 shows Q^{-1} (for P-waves) as a function of frequency with only one relaxation mechanism and the frequency spectrum of a representative source. The Q^{-1} curve has one apex, and we can set its position to coincide with the dominant frequency of the source. Thus, the part of the source that has the most energy also has the strongest attenuation; other frequencies correspond to weaker attenuations. The apex value of the Q^{-1} curve (at $Q^{-1} \approx 0.5$) in Figure 1 is sufficient to attenuate the P-wave quickly. Field data often have a nearly flat spectrum in the seismic frequency range, and using more relaxation mechanisms for attenuation is an option to better fit the data frequency spectrum; the computational cost will be increased correspondingly. If the shape of the spectral function used to attenuate the P- or S-waves does not match that of the data, it will take more time steps to achieve decomposition, but it will still work. Decreasing Q also increases the phase velocity at high frequencies (Carcione et al., 1988a), which may cause numerical instability problems when using finite-difference schemes for wavefield extrapolation; the computational grid increment and time step can be adjusted to ensure stability.

There are different methods for parameterization of viscoelastic moduli. Carcione et al. (1988a, 1988b) and Carcione (1993) use relaxed (and unrelaxed) bulk and shear moduli to describe the model; Robertsson et al. (1994) use P- and S-wave moduli. Because of the differences in parameterizations, the details of the calculations for the memory variables are also different. However, for the purpose of P and S decomposition, we choose to parameterize the model with P- and S-wave moduli, in which case, the memory variables can be grouped into P- and S-parts. The algorithm of selective attenuation can be deduced from the viscoelastic constitutive equations, for an isotropic 2D medium (Robertsson et al., 1994), that relate stresses and particle velocities. Thus,

$$\frac{\partial \sigma_{xx}}{\partial t} = M_{1u}\left(\frac{\partial v_x}{\partial x} + \frac{\partial v_z}{\partial z}\right) - 2M_{2u}\frac{\partial v_z}{\partial z} + e_{11}, \tag{5}$$

$$\frac{\partial \sigma_{zz}}{\partial t} = M_{1u}\left(\frac{\partial v_x}{\partial x} + \frac{\partial v_z}{\partial z}\right) - 2M_{2u}\frac{\partial v_x}{\partial x} + e_{22}, \tag{6}$$

and

$$\frac{\partial \sigma_{xz}}{\partial t} = M_{2u}\left(\frac{\partial v_x}{\partial z} + \frac{\partial v_z}{\partial x}\right) + e_{12}. \tag{7}$$

The memory variables e_{ij} in equations 5–7 are obtained recursively over time steps from

$$\frac{\partial e_{11}}{\partial t} = \frac{1}{\tau_\sigma}(M_{1r} - M_{1u})\left(\frac{\partial v_x}{\partial x} + \frac{\partial v_z}{\partial z}\right) - \frac{2}{\tau_\sigma}(M_{2r} - M_{2u})\frac{\partial v_z}{\partial z} - \frac{e_{11}}{\tau_\sigma}, \tag{8}$$

$$\frac{\partial e_{22}}{\partial t} = \frac{1}{\tau_\sigma}(M_{1r} - M_{1u})\left(\frac{\partial v_x}{\partial x} + \frac{\partial v_z}{\partial z}\right) - \frac{2}{\tau_\sigma}(M_{2r} - M_{2u})\frac{\partial v_x}{\partial x} - \frac{e_{22}}{\tau_\sigma}, \tag{9}$$

and

$$\frac{\partial e_{12}}{\partial t} = \frac{1}{\tau_\sigma}(M_{2r} - M_{2u})\left(\frac{\partial v_x}{\partial z} + \frac{\partial v_z}{\partial x}\right) - \frac{e_{12}}{\tau_\sigma}. \tag{10}$$

Here, M_{1r} and M_{2r} are relaxed (elastic) moduli for P- and S-waves (indicated by subscripts 1 and 2, respectively), M_{1u} and M_{2u} are the corresponding unrelaxed (viscoelastic) moduli, σ_{ij} is stress, v_i is the ith component of the particle-velocity vector, and τ_σ is the stress relaxation time.

The above formulation simulates attenuation of P- and S-waves, but to realize the P and S wavefield decomposition, we need to preserve one wave mode during extrapolation. We manipulate the formulation to make the energy dissipation occur only for one wave mode by making $M_{1r} = M_{1u}$ or $M_{2r} = M_{2u}$, and thereby decomposing the P- and S-waves. The viscoelastic formulation leads to dispersion as well as attenuation; however, the associated dispersion can be disregarded as long as it does not cause a numerical instability problem because it occurs only in the wave mode that is being attenuated.

To realize the P and S vector decomposition, we can choose to attenuate either P- or S-waves, but we find that P-wave attenuation is more efficient because, if all the S-wave moduli are elastic ($M_{2r} = M_{2u}$), then only one memory variable is needed (in 2D and 3D), which is much faster and more efficient than solving the original viscoelastic wave equations. In contrast, attenuating the S-waves requires that three memory variables be calculated in 2D and six in 3D. As a result, we use only P-wave attenuation to represent the selective attenuation method in the following tests and comparisons. To attenuate the P-waves, we define a new memory variable e_{PP} at each grid point by

$$\frac{\partial e_{\mathrm{PP}}}{\partial t} = \frac{1}{\tau_\sigma}(M_{1r} - M_{1u})\left(\frac{\partial v_x}{\partial x} + \frac{\partial v_z}{\partial z}\right) - \frac{e_{\mathrm{PP}}}{\tau_\sigma}; \tag{11}$$

thus, the 2D memory variables can be simplified to

$$e_{11} = e_{22} = e_{\mathrm{PP}} \tag{12}$$

and

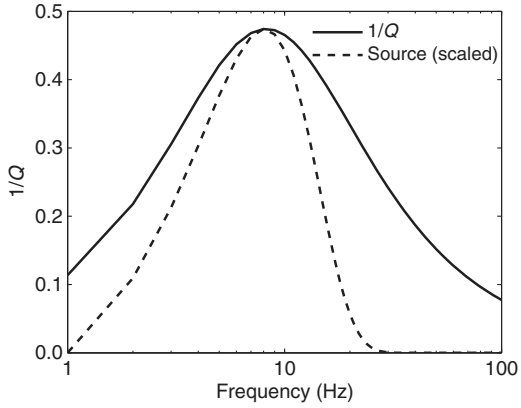

Figure 1. P-wave Q^{-1} as a function of frequency with one relaxation mechanism (the solid line) and the frequency spectrum of the source (the dashed line).

$$e_{12} = 0. \tag{13}$$

With strong attenuation of the P-waves, after a few time steps, the extrapolated wavefields contain only S-waves in all particle velocity and stress components. To get the decomposed P-waves, a complete elastic extrapolation needs to be performed concurrently, and the particle-velocity components of the P-waves are obtained by subtraction of the preserved S wavefield from the complete propagating elastic particle-velocity wavefield at the same time step.

Decoupled propagation

Decoupled propagation is based on the assumption, implementation, and application of a decoupled isotropic elastic extrapolation. Ma and Zhu (2003) apply the elastic numerical solution for decoupled P- and S-waves in a pseudospectral solution. Zhang et al. (2007) and Xiao and Leaney (2010) use 2D staggered-grid, stress-particle velocity formulations with a similar idea to decompose the elastic wavefield. Following Xiao and Leaney (2010), the stress-particle velocity formulation of the elastodynamic equations for decoupled isotropic elastic propagation is

$$\frac{\partial \sigma_{xx}}{\partial t} = \left[(\lambda + 2\mu)\left(\frac{\partial v_x}{\partial x} + \frac{\partial v_z}{\partial z}\right)\right] - 2\mu\frac{\partial v_z}{\partial z}, \tag{14}$$

$$\frac{\partial \sigma_{zz}}{\partial t} = \left[(\lambda + 2\mu)\left(\frac{\partial v_x}{\partial x} + \frac{\partial v_z}{\partial z}\right)\right] - 2\mu\frac{\partial v_x}{\partial x}, \tag{15}$$

$$\frac{\partial \sigma_{zx}}{\partial t} = \mu\left(\frac{\partial v_x}{\partial z} + \frac{\partial v_z}{\partial x}\right), \tag{16}$$

$$\frac{\partial v_x}{\partial t} = \frac{1}{\rho}\left(\frac{\partial \sigma_{xx}}{\partial x} + \frac{\partial \sigma_{zx}}{\partial z}\right), \tag{17}$$

and

$$\frac{\partial v_z}{\partial t} = \frac{1}{\rho}\left(\frac{\partial \sigma_{zx}}{\partial x} + \frac{\partial \sigma_{zz}}{\partial z}\right), \tag{18}$$

where σ_{ij} is the stress, v_i is the particle velocity, and λ and μ are Lamé parameters.

The time derivative of the normal stress (in the square brackets in equations 14 and 15) corresponds to the P-wave stress, so it can be calculated separately and given the new notation σ_P, to replace σ_{xx} and σ_{zz}, where

$$\frac{\partial \sigma_P}{\partial t} = (\lambda + 2\mu)\left(\frac{\partial v_x}{\partial x} + \frac{\partial v_z}{\partial z}\right). \tag{19}$$

The P-wave particle-velocity components v_{xP} and v_{zP} are calculated from σ_P from equations 17 and 18 by finite differencing to give

$$\frac{\partial v_{xP}}{\partial t} = \frac{1}{\rho}\frac{\partial \sigma_P}{\partial x} \tag{20}$$

and

$$\frac{\partial v_{zP}}{\partial t} = \frac{1}{\rho}\frac{\partial \sigma_P}{\partial z}. \tag{21}$$

This gives a complete decomposition of the P-wavefield, and, similar to the selective attenuation method, we can get the S-wavefield by subtracting the P-wavefield from the complete wavefield component by component, so

$$v_{xS} = v_x - v_{xP} \tag{22}$$

and

$$v_{zS} = v_z - v_{zP}. \tag{23}$$

The decoupled propagation obtains the P-waves by using the divergence operator that already exists within the elastodynamic wave equations 14 and 15, via equations 19–21, so the decomposition process is a part of the wavefield propagation process, and the amplitude and phase are accurately preserved. Zhang et al. (2007) use a different form of the decoupled equations, which can be proven to be equivalent to equations 19–23 (see Appendix A).

TEST WITH SYNTHETIC DATA

In this section, the selective attenuation and decoupled propagation are tested with data from two different elastic models, together with a test on data from a homogeneous elastic model using divergence and curl operators to demonstrate the advantages of vector decomposition. For all of the following tests, we use a 2D staggered-grid finite-difference solution (Virieux, 1986) to solve the stress-particle velocity formulation of the elastodynamic equations. The advantage is that it does not use derivatives of the elastic moduli, and thus it is more efficient and accurate than the traditional nonstaggered elastic wave equation. We use eighth-order finite-difference equations to calculate spatial derivatives at each grid point within the model including the edges; there will not be any significant edge reflections because convolutional perfectly matched layer absorbing boundary conditions (Komatitsch and Martin, 2007) with a width of 20 grid points inside the model are used on all four grid edges. To have enough grid points for eighth-order finite differencing of the derivatives in the elastodynamic equations, the virtual top of the model is defined at the fifth grid point at depth z below the inner bound of the top absorbing layer.

The first 2D test is performed on a 256×256 homogeneous isotropic elastic model with grid increments $h = 5$ m and time increments $dt = 0.5$ ms. A composite source, which generates both P- and S-waves simultaneously, is placed at the center of the grid. Figure 2a shows snapshots of the resulting elastic wavefield at five different times. The P- and S-waves are propagating at different velocities and have different polarizations in their horizontal and vertical components.

We first separate the P and S-waves in the 2D, 2C elastic wavefield (Figure 2a) using divergence and curl operators (Figure 2b). The P and S separation is good, but the original 2C (x and z) elastic wavefield becomes one component for P and one for S. The P-wave becomes a scalar wavefield, and the S-wave becomes a vector wavefield with only one nonzero component; the original vector component information is lost. Without the amplitude correction using

equation 3, and the 90° phase correction, the phase and amplitude information are changed from those in the input data.

Decomposition by selective attenuation

Next, we change the medium from elastic to viscoelastic with strong attenuation of P-waves using $Q^{-1} \approx 0.5$ as shown in Figure 1. Because the P-waves are attenuated quickly, the snapshots in Figure 3b are the decomposed S-wavefield. The subtraction of Figure 3b from Figure 2a gives the decomposed vector P-wavefield snapshots in Figure 3a.

Decomposition by decoupled propagation

Figure 4 shows the decomposed P- and S-waves using decoupled propagation. Compare these with the snapshots calculated by selective attenuation in Figure 3; even though they use different methods, these methods yield very similar, clean, and accurate decomposition

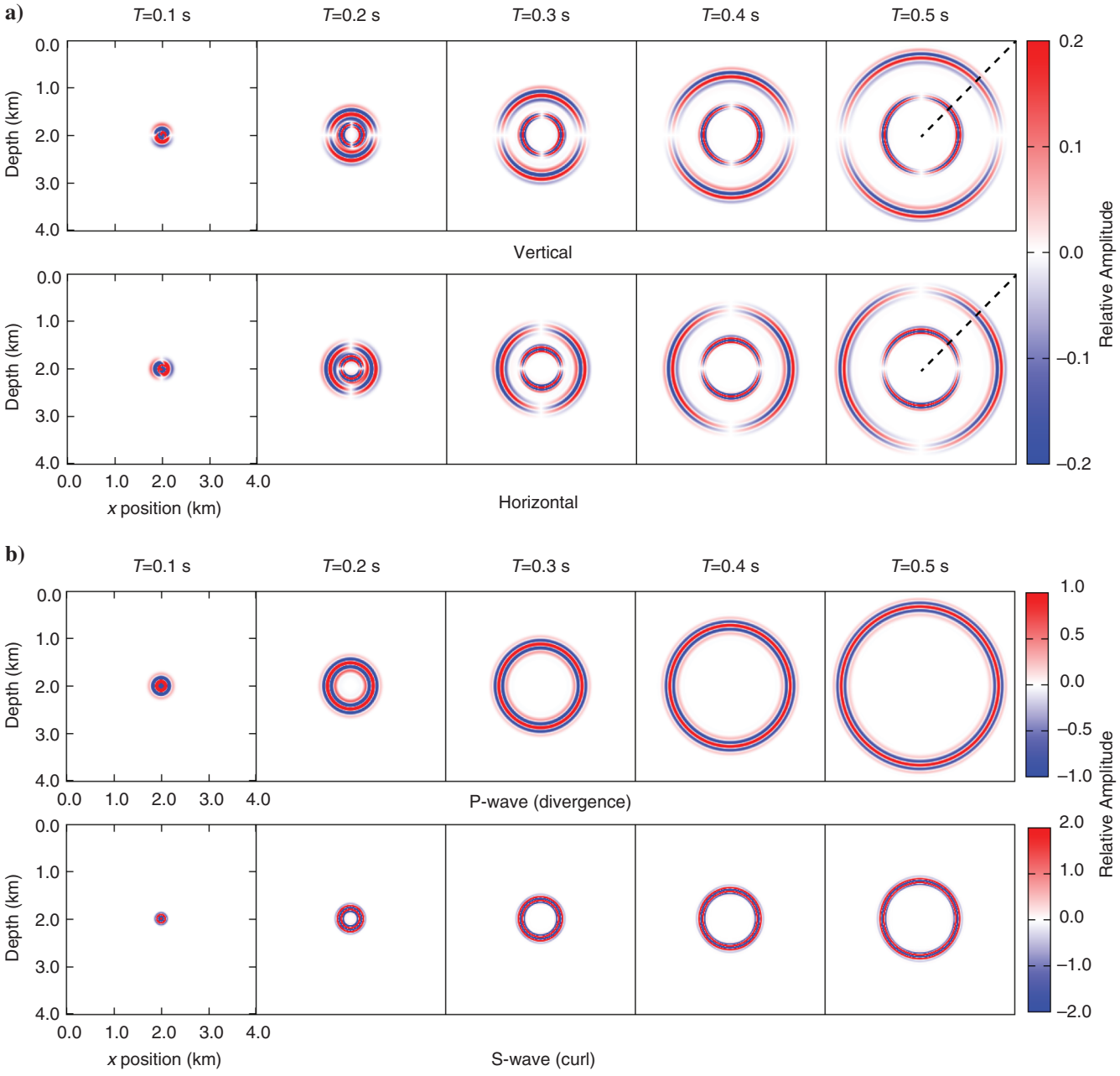

Figure 2. (a) Snapshots of 2D wave propagation in an elastic homogeneous medium with a composite P and S source at the center. The vertical and horizontal components of the wavefields are recorded. (b) Separation results with the divergence (upper panels) and the curl (lower panels) operators. Note the large differences in the relative amplitudes between (a) and (b) because they are not the same physical waves. Amplitudes along the dashed lines here and in Figures 3 and 4 are shown in Figure 5.

results for the P- and S-waves. The main difference is that some small residuals remain in the first snapshots of selective attenuation because attenuation (no matter how strong) cannot be achieved instantly. In Figures 3 and 4, the vertical and horizontal components of the elastic wavefields are preserved in the decomposition, and there are no phase or amplitude changes, so no corrections are needed.

EVALUATION OF ALGORITHM PERFORMANCE

Selective attenuation and decoupled propagation decompose the wavefield into their respective P- and S-vector components. It will be valuable to know which is more suitable for application; the comparisons below are performed to evaluate accuracy, speed, memory requirements, and numerical stability.

Accuracy

We consider accuracy to be the most important basis for evaluation of the decomposition methods. To provide a criterion to test the accuracy of the decomposition results, we return to the simulation in Figure 2a, but the source is changed to an explosive source to generate pure P-wave snapshots, and then it is changed to a shear source to get pure S-wave snapshots at the same time steps as those

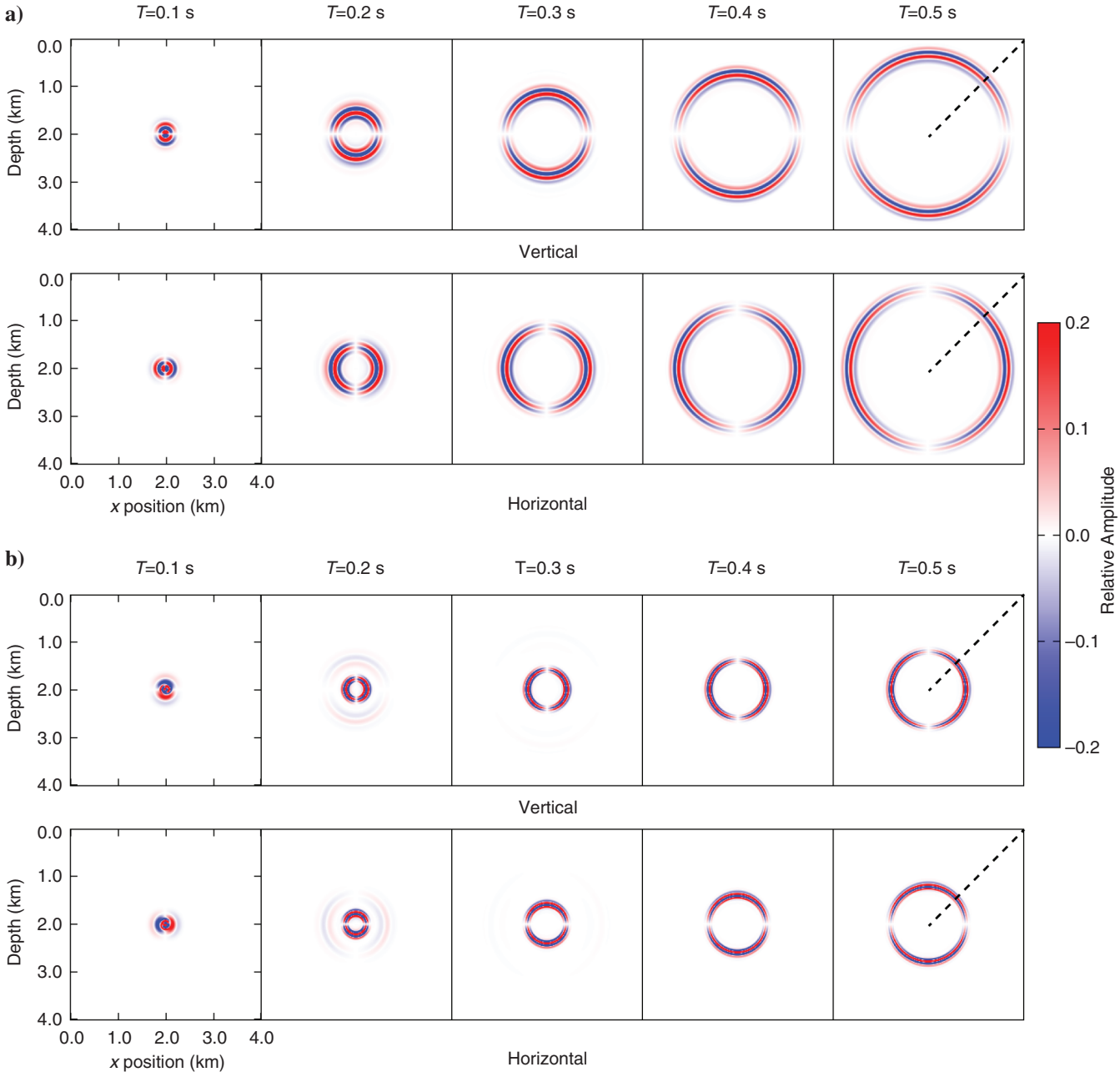

Figure 3. Snapshots of wave propagation in a viscoelastic medium with strong P-wave attenuation. (a) Decomposed P-waves and (b) decomposed S-waves. Compare with Figures 2 and 4.

shown in Figure 2a. Because the medium is homogeneous, no conversions occur during the elastic wavefield extrapolation. If the decomposition is accurate, the results should be the same as those generated in the pure P- or S-wave snapshots, and the residual can be used as a quantitative measure of accuracy.

We define the wavefield residual to be the sum of the absolute value over all grid points and components, of the difference between the pure-wave-mode P and S particle-velocity snapshots and the corresponding decomposed P and S snapshots. In Figure 5, the pure P- or S-waves (the dashed red lines) are plotted along with the decomposition results (the solid blue lines), for both decomposition methods, extracted along the dashed line trajectories in Figures 2a, 3, and 4. The good match between the pure and the decomposed waves indicates the absolute accuracy of the decomposed waves and the equivalent accuracy for both decomposition algorithms; the overlain blue and red lines are visually indistinguishable.

Figure 6 shows the particle-velocity residuals in the homogeneous medium; the residuals in inhomogeneous media are similar. Because the attenuation method cannot decompose the wavefields instantly, compared with decoupled propagation, the selective attenuation needs more time steps to complete the vector

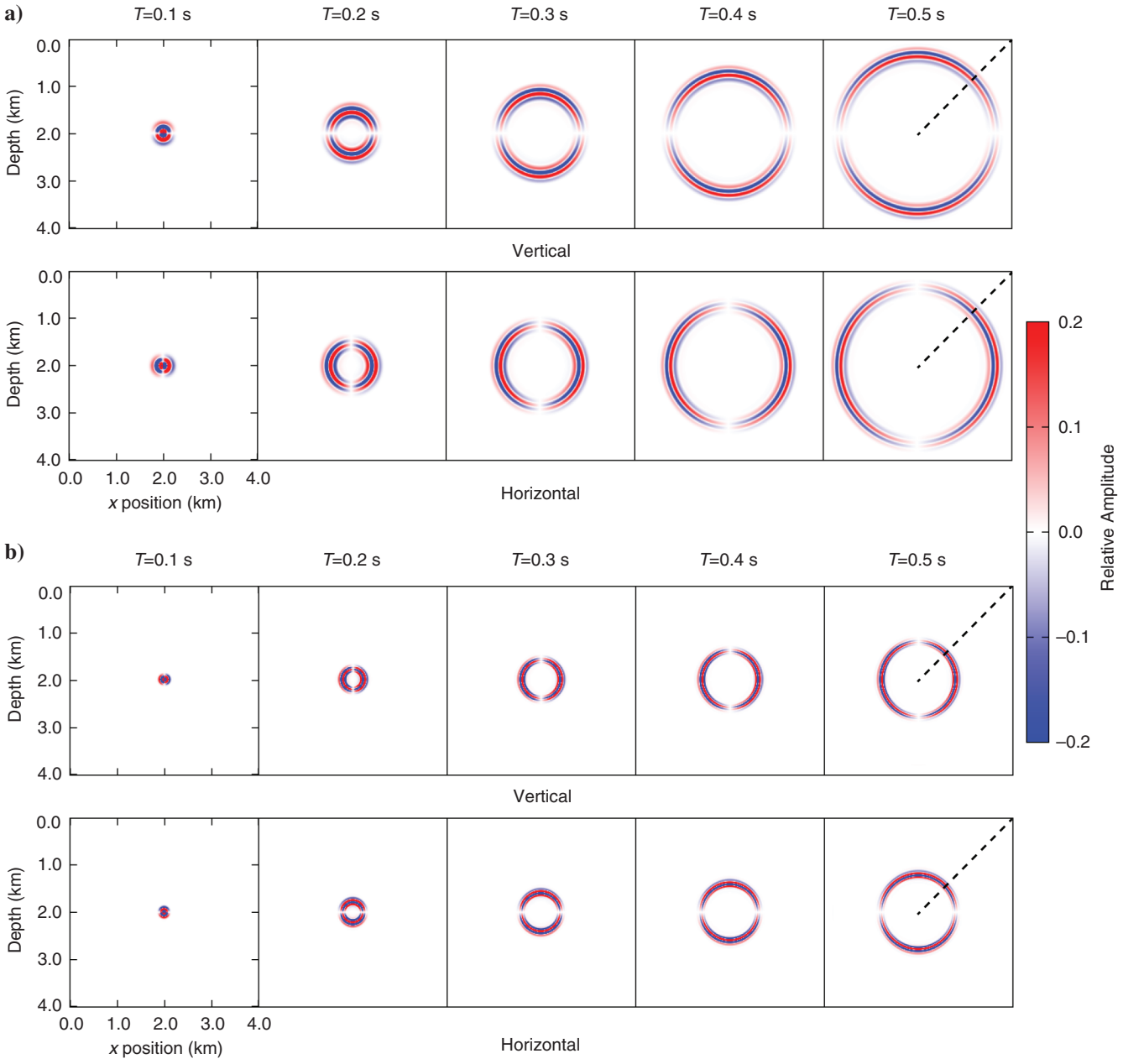

Figure 4. Decomposed snapshots of wave propagation using decoupled propagation: The (a) decomposed P-wavefield and (b) decomposed S-wavefield. Compare these with Figures 2 and 3.

decomposition. The decoupled propagation has near-zero residuals from the beginning.

Both vector decompositions are effective in an inhomogeneous velocity model provided that the model is sufficiently smoothed to avoid generation of reflections, converted waves, and head waves during the extrapolations. The presence of these secondary waves is particularly undesirable in the context of subsequent application of RTM, where they produce artifacts. To illustrate, consider the simple elastic model in Figure 7a, which has a single flat reflector at 2.6 km depth. A rotational source, located at $(x, z) = (2.0, 2.0)$ km generates only S-waves that, as they hit the reflector, produce S-to-P converted waves and evanescent (head) waves as well as reflected waves (Figure 8a). Applying the decomposition algorithms to these (forward-propagating) waves produces the snapshots at 0.5 s shown in Figure 8a. The dashed ovals indicate the positions of the S-to-P-wave conversions and S-wave reflections at the reflector. Figure 8b shows the same information, obtained using the smoothed velocity model in Figure 7b; the

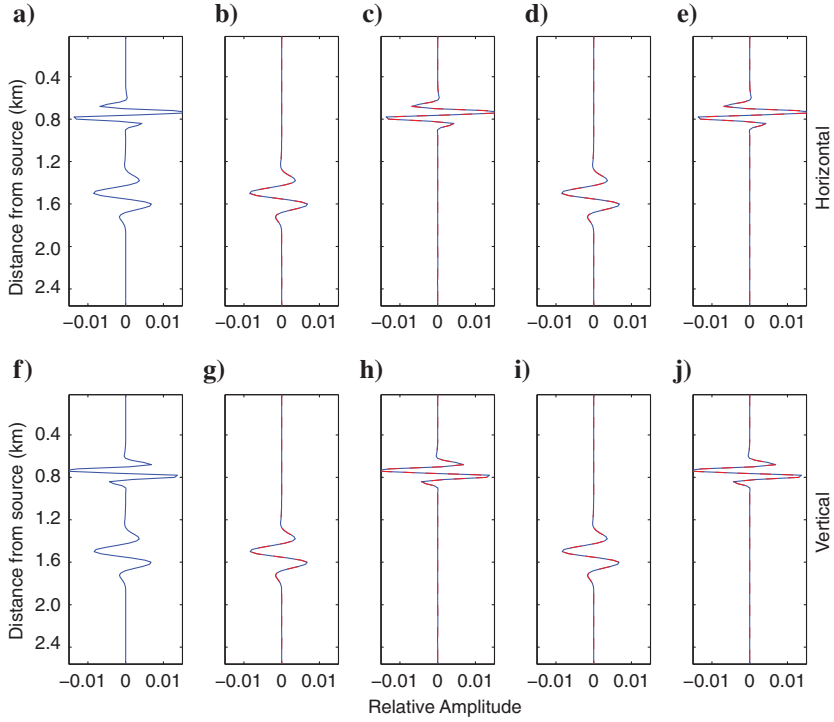

Figure 5. Comparison of waveforms along the dashed lines in Figures 2a, 3, and 4 at 0.5 s. Panels (a and f) are horizontal and vertical components of the elastic wavefield (without vector decomposition) from Figure 2a. Panels (b and g) contain the P-waves, and panel (c and h) contain the S-waves, both decomposed using selective attenuation (the solid blue lines) and the pure P- and S-waves (the dashed red lines), respectively. Panels (d and i) contain the P-waves, and panels (e and j) contain the S-waves, both decomposed using decoupled propagation (the solid blue lines) and the pure P- and S-waves (the dashed red lines), respectively.

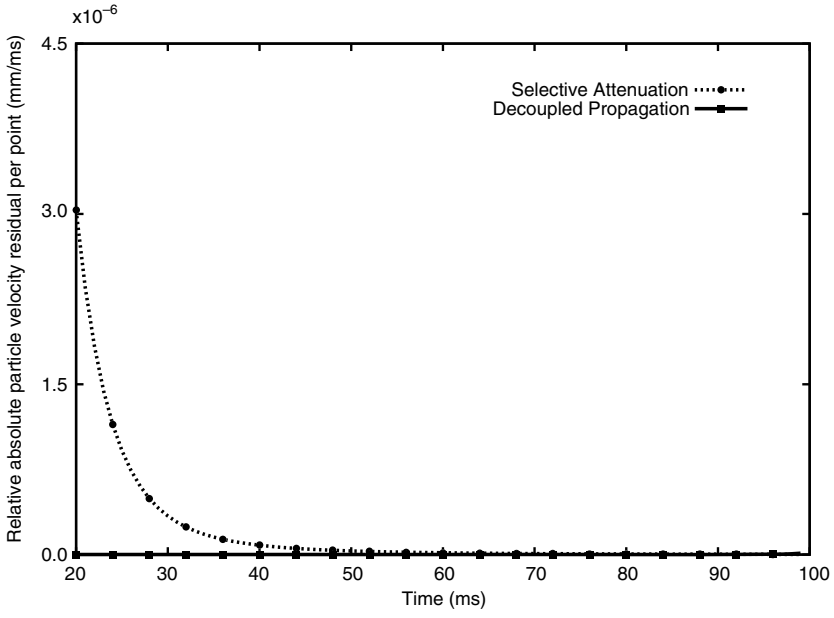

Figure 6. The dotted line shows the residuals using the selective attenuation (of P-waves). The solid line shows the residuals using decoupled propagation.

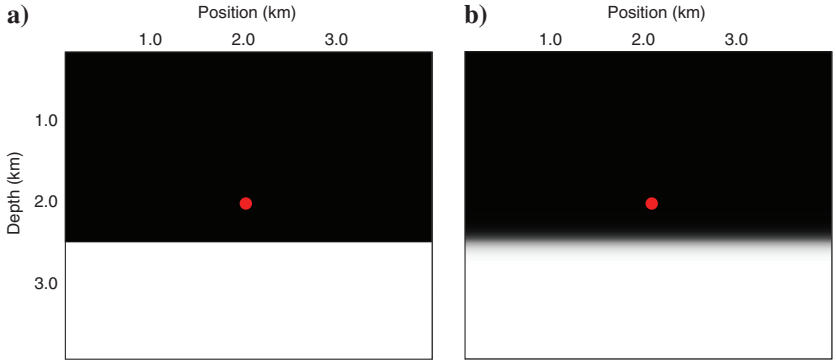

Figure 7. (a) True and (b) smoothed velocity model for elastic wavefield extrapolation and P and S decomposition. The red dots are rotational sources. In panel (a), the upper layer has P- and S-velocities of 1.70 and 1.20 km/s, and the lower layer has P- and S-velocity of 1.90 and 1.40 km/s.

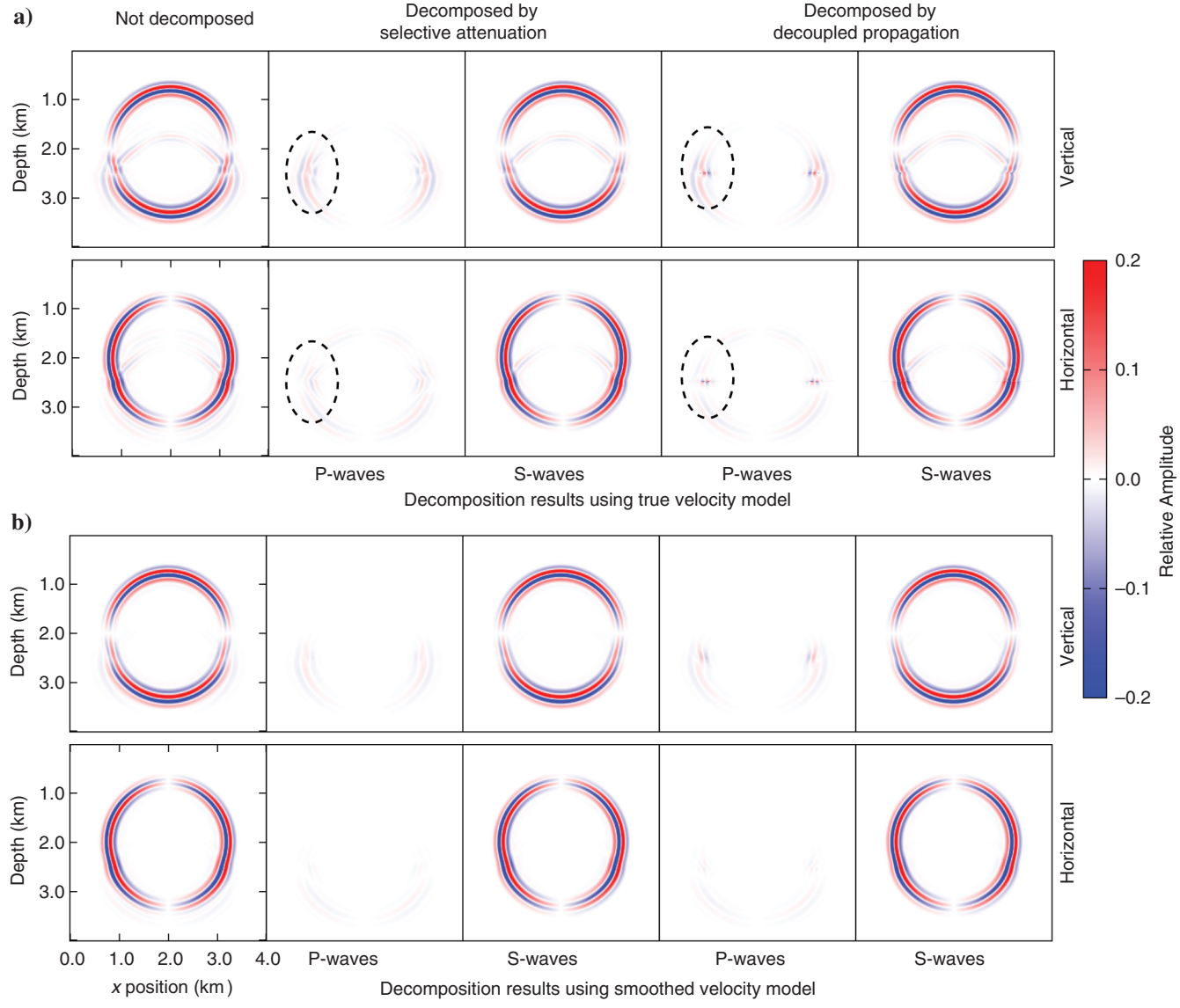

Figure 8. Snapshots at 0.5 s of the elastic wavefield and P and S decomposition results in a model with one horizontal reflector at (a) $z = 2.6$ km, and (b) the corresponding smoothed model. The models are shown in Figure 7. In panels (a and b), the leftmost pair contains the vertical and horizontal components of the elastic wavefield (without decomposition) and the next two pairs contain the decomposed P- and S-waves using selective attenuation. The two rightmost pairs contain the decomposed P- and S-waves using decoupled propagation. The sources for both decompositions are rotational and generate only S-waves. Conversions to P-waves occur at the reflector if using the true velocity model. Selective attenuation and decoupled propagation decompositions produce artifacts (in the dashed ovals) at the reflector in panel (a) because of the coupling of P- and S-waves and the generation of head waves, but these artifacts are much reduced when using the smoothed velocity model in panel (b).

artifacts produced by both decomposition algorithms are smaller in the smoothed model.

Speed

Time efficiency is a key consideration for commercial applications. The selective attenuation and decoupled propagation vector decomposition methods are embedded in the extrapolations, which means that both are more costly than solving only the elastic wavefield extrapolation. We evaluate the relative time efficiency of the attenuation and decoupled algorithms by comparing their computation times (including decomposition), with the time for elastic extrapolation alone (without decomposition). The central processing unit used is a single-core AMD Phenom™ 9850 quad-core 2.6 GHz processor. Figure 9 shows the time consumed by each method for three different grid sizes. The decoupled propagation has better time efficiency than selective attenuation by approximately a factor of two, mainly because selective attenuation needs a second (elastic) extrapolation if the decomposed P- and S-waves are needed.

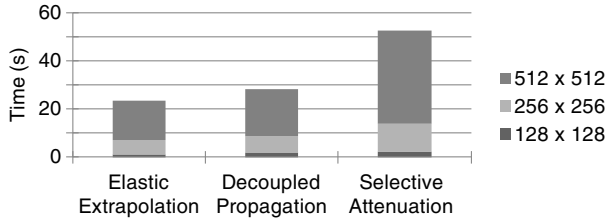

Figure 9. Time-efficiency comparison for three grid sizes.

Table 1. Variables required for 2D vector decomposition algorithms and elastic wavefield extrapolation (M_{2u} is not included in the selective attenuation column as $M_{2u} = M_{1u}$).

Methods	Elastic extrapolation	Decoupled propagation	Selective attenuation
Variables	λ, μ, ρ σ_{xx}, σ_{zz}, σ_{zx} v_x, v_z	λ, μ, ρ σ_{xx}, σ_{zz}, σ_{zx} v_x, v_z v_{Px}, v_{Pz}, σ_P	M_{1r}, M_{2r}, M_{1u}, ρ σ_{xx}, σ_{zz}, σ_{zx} v_x, v_z, v_{Sx}, v_{Sz} σ_{xxq}, σ_{zzq}, σ_{zxq}, e_{PP}
Total number	8	11	15

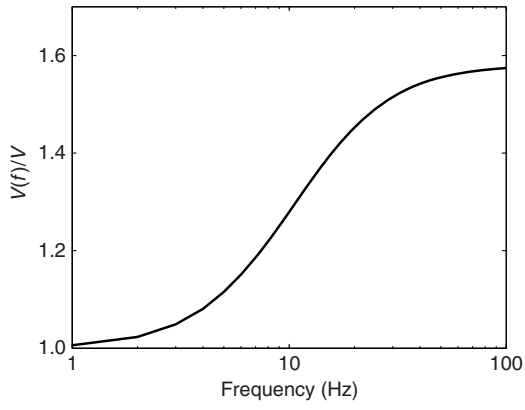

Figure 10. The ratio of wave velocities as a function of frequency in a homogeneous viscoelastic medium $[V(f)]$ and in the elastic medium V with the same relaxed (elastic) modulus M_{1r}.

Memory requirement

The memory occupied by elastic wavefield extrapolation with vector decomposition is larger than without decomposition (Table 1). If the output wavefields are the decomposed particle-velocity vectors, then we need to store at least one additional 2C elastic wavefield per time step: The decomposed P or S vector wavefield (the other wave mode can be obtained by subtraction) no matter what vector decomposition method we choose. Additional memory might be necessary depending on the algorithms. The P-wave stress grid σ_P, as used in decoupled propagation, also needs to be saved during wavefield extrapolation. For selective attenuation (only P-wave attenuation is considered in this section), one value of the memory variable e_{PP} needs to be stored for each grid point. To obtain the decomposed P- and S-wave modes, a complete elastic extrapolation needs to be carried out simultaneously with the viscoelastic extrapolation for subtraction at each time step; thus, the numbers of particle velocities and stresses are doubled, and we use the suffix q, after the viscoelastic stresses, to distinguish from the elastic ones in Table 1.

Because Q is only a processing parameter, a fixed relaxation time is used for all grid points to save RAM storage. The total size of the memory needed is proportional to the number of wavefields and the size of each wavefield. Table 1 shows the number of variables that need to be kept in RAM by each wavefield-decomposition algorithm; in 2D, the selective attenuation needs 27% more RAM than decoupled propagation.

Because wavefield extrapolation with selective attenuation implemented gives only one wave mode (P or S) depending on which is attenuated, and we use subtraction to get the other wave mode, the complete elastic wavefield without decomposition also needs to be computed. However, if only one wave mode is needed for later processing, then the elastic wavefield without decomposition is no longer required, and the computational cost is correspondingly reduced.

Numerical stability

The stability criterion influences how we choose the extrapolation parameters. Although selective attenuation and decoupled propagation are embedded in extrapolation, they have different stability criteria as they involve finite-difference solutions of different equations. Because of the velocity dispersion in the viscoelastic scheme used in the selective attenuation algorithm, the stability criterion has to be computed using the highest phase velocity $v_{max} = \sqrt{\frac{M_{1u}}{\rho}}$, which is obtained at infinite frequency (Dablain, 1986; Levander, 1988; Robertsson et al., 1994), so the stability depends on the amount of attenuation that is applied for decomposition. Figure 10 shows the ratio of P-wave velocities in a homogeneous viscoelastic medium of velocity $V(f)$ (which is a function of frequency f), to the constant velocity V in the corresponding elastic medium. For the attenuation curve in Figure 1,

the maximum viscoelastic P-wave velocity becomes approximately 1.6 times the maximum elastic P-wave velocity, thus making it more expensive to satisfy the stability criterion. As shown in Figure 1, using a low-Q would make the attenuation of the unwanted waves more efficient, but it would require a finer grid increment to insure stability. So, the optimal combination is model dependent.

Comparison using Marmousi2 data

To demonstrate that selective attenuation and decoupled propagation work in inhomogeneous as well as homogeneous media, a more salient test is performed on data from a part of the 2D elastic Marmousi2 model (Figure 11). The original model is redefined with grid increments $h = 5$ m. The composite (P and S) source is placed at $z = 0.3$ and $x = 1.6$ km; the water layer at $z < 0.3$ km is replaced with an absorbing zone and is not shown in the snapshots. The time increment in the extrapolation is $dt = 0.5$ ms. Figure 12a and 12b shows a snapshot of the elastic particle-velocity wavefield components before decomposition. The parameter models (λ, μ, and density) need to be smoothed to do the decomposition so there are no extra reflected or converted waves produced during extrapolation (which is also a prerequisite in RTM to reduce migration artifacts). Figure 12c, 12e, 12g, 12i and 12d, 12f, 12h, 12j show the decomposed P- and S-wave horizontal and vertical component snapshots obtained using selective attenuation and decoupled propagation. Selective attenuation and decoupled propagation effectively decompose the P- and S-waves into their vertical and horizontal components. These methods would work similarly well in three dimensions.

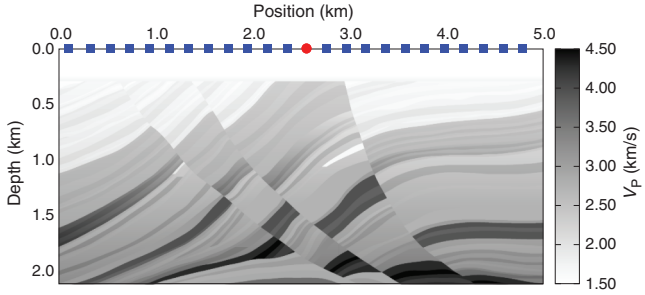

Figure 11. A subset of the elastic Marmousi2 P-wave velocity model; the red dot is the source location used for the x-t gather decomposition example, and the blue squares are every 40th receiver.

P AND S DECOMPOSITION IN x- t GATHER DATA

To generate decomposed P- and S-wavefields from recorded 2C x-t-domain data, an additional step can be performed after P and S decomposition of a receiver wavefield in the space domain, as described by Sun and McMechan (2001). The P- and S-wavefields can be saved during the downward extrapolation in the space domain at a line of virtual receivers and then input into upward extrapolations of the P- and S-wavefields, separately, to reconstruct a P-wave and an S-wave in the (x, z, and t) data domain. Sun and McMechan's (2001) implementation uses divergence and curl, but we can now do the decomposition with either of the vector algorithms, so that the amplitude and phase of the vector components are decomposed and preserved.

We use a homogeneous model for the extrapolations so there will be no mode conversions, and the model needs to be solid to propagate S-waves as well as P-waves. Any effects of the downward extrapolation in the homogeneous model will be undone in the

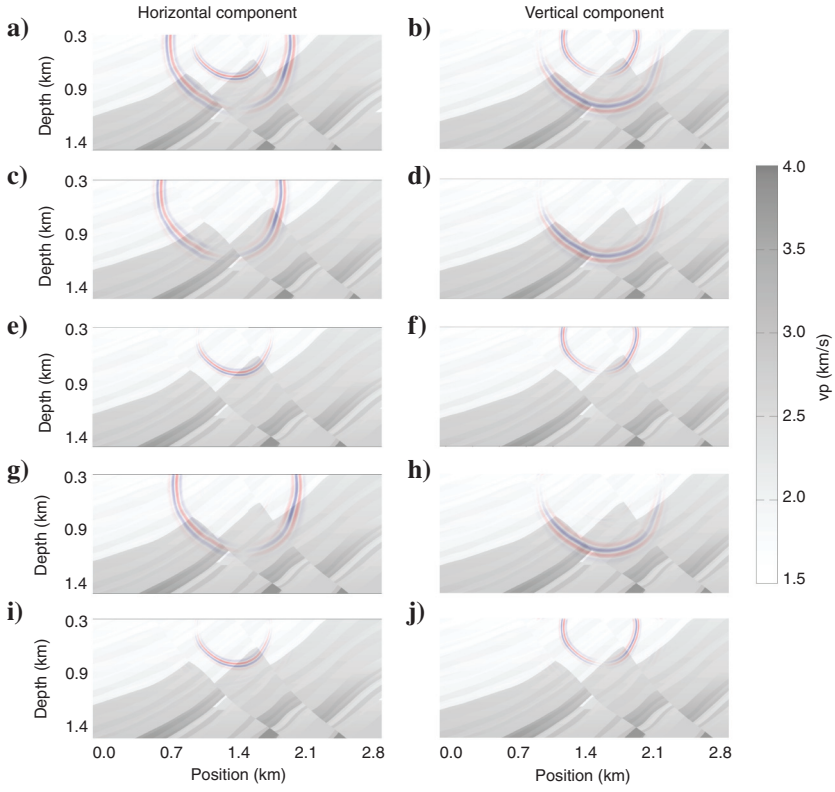

Figure 12. Snapshots of the wave propagation in a portion of the elastic Marmousi2 model in Figure 11 at time = 0.75 s, using the true P-wave velocity model as the background with wavefield snapshots overlapped with 50% transparency. All snapshots are particle-velocity components; panels (a, c, e, g, and i) are v_x and panels (b, d, f, h, and j) are v_z. Panels (a and b) are the complete elastic particle-velocity wavefield without P and S decomposition, panels (c and d) are the decomposed Pwavefield using selective attenuation, panels (e and f) are the decomposed S-wavefield using selective attenuation, panels (g and h) are the decomposed P-wavefield using decoupled propagation; and panels (i and j) are the decomposed S-wavefield using decoupled propagation.

subsequent upward extrapolation, so the decomposition results are not sensitive to the elastic model used for the extrapolations. We can choose either selective attenuation or decoupled propagation for the decomposition algorithm. Because the decoupled propagation has better efficiency and does not have a time requirement to complete decomposition (Figure 6), we apply only the decoupled propagation to do the decomposition for the x-t data in this example. We use the 2C particle velocity as the input seismogram for downward and upward extrapolations. The stress components are not required for boundary conditions as long as their values are sufficiently small at the last time step (Nguyen and McMechan, 2015); after a few time steps of reconstruction, the stress components, computed from the particle velocities, will be consistent with the particle velocities via equations 14–21. The procedure is as follows:

1) Downward extrapolation of a source gather (a 2C particle-velocity seismogram) into a homogeneous solid medium. The decoupled elastic wave equations 14–21 are used to obtain stresses and particle velocities iteratively for elastic wavefield extrapolation; the calculation of the S-wave particle velocities in equations 22 and 23 can be omitted because the S-wave seismogram can be obtained by subtraction in step 3 (below) after the P-wave components are decomposed.
2) We save the P-wave particle velocities as time-slice seismograms, at a line of virtual subsurface receivers below the true receivers, to be used in the P-S decomposition. The depth of the virtual receivers $z \geq 4h$ (where h is the grid increment); another four grid points that are needed for eighth-order finite differencing in the z-direction lie above the true receiver line. Four grid points are enough for decomposition using decoupled propagation because with this method, the decomposition occurs instantaneously; more are needed when using selective attenuation, depending on the amount of attenuation being applied.
3) We use the P-wave particle-velocity seismogram saved at the virtual receivers for use in boundary conditions to upward extrapolate the wavefield; the original elastic wavefield extrapolator (equations 14–18) can be used because the medium is homogeneous, the upward extrapolated wavefield contains only P-waves, and no conversions will occur. Then, the P-wave particle-velocity seismogram is recorded at the same time steps and receiver positions as the original seismogram, and subtraction of the P-wave seismogram from the original seismogram yields the decomposed S-wave particle-velocity seismogram.

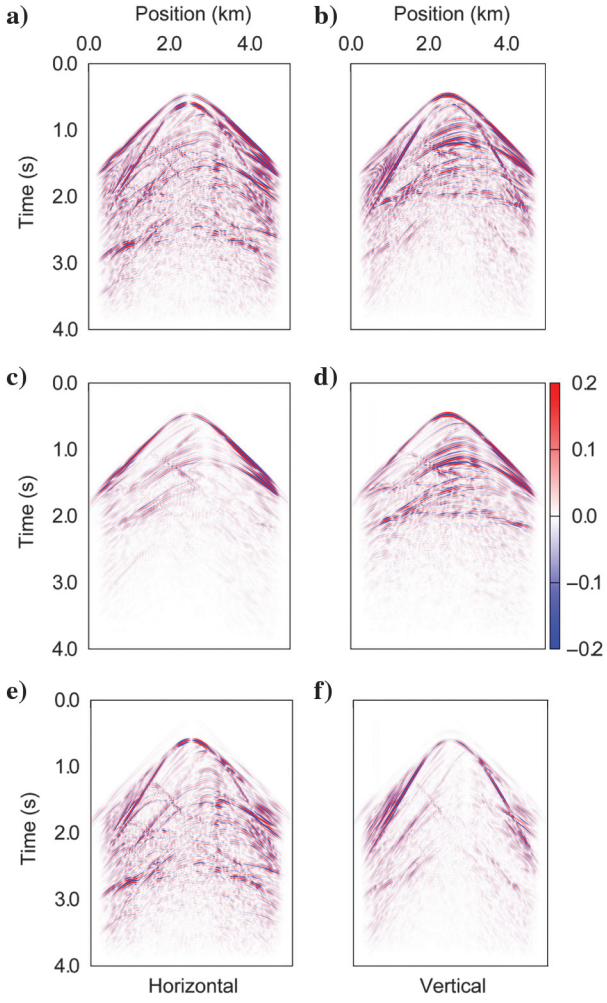

Figure 13. Panels (a and b) are the recorded seismogram generated from the Marmousi2 model with the direct waves removed, panels (c and d) are the decomposed P-wave seismogram, and panels (e and f) are the decomposed S-wave seismogram. In each pair, panels (a, c, e) are the horizontal component and panels (b, d, f) are the vertical component.

As an example, we use decoupled propagation to demonstrate the P and S vector decomposition of x-t data for a part of the Marmousi2 model (Figure 11). An explosive source with a dominant frequency of 15 Hz is placed at the position $(x, z) = (2.5, 0.0)$ km. The grid increments are redefined to be $h = 5$ m in the x- and z-directions. The time-sampling increment $\Delta t = 0.5$ ms; 1001 receivers with spacing 5 m are placed at a depth $z = 0.0$ km, and the virtual receivers are placed at a depth $z = 0.02$ km with spacing 5 m. Figure 13a shows the recorded seismograms from forward modeling. Figure 13 shows the recorded elastic seismogram from forward modeling and its decomposition into 2C P- and S-wave seismograms.

DISCUSSION

Besides the many advantages of vector decomposition, the decomposed elastic wavefield vectors contain polarization information that can be directly related to propagation angles: P-wave particle velocity (or displacement) is parallel to the propagation direction, and S-wave particle velocity (or displacement) is normal to the propagation direction. This provides a possible foundation for calculating propagation angles, which facilitates the subsequent procedure of obtaining ADCIGs during RTM.

The vector decomposition methods provide complete and accurate information in the decomposed wavefields, but it comes with a price; attenuation and decoupled vector decomposition methods are more expensive than calculating the divergence and curl operators. The decomposed wavefields and seismograms preserve all their original information in vector form, so they cannot be accurately processed with acoustic (1C) processing software. A caution for using selective attenuation and decoupled propagation is that they require the extrapolation model to be smoothed enough to avoid any secondary reflections or mode conversions during the extrapolation performed for decomposition, but this is already commonly used in RTM (Chattopadhyay and McMechan, 2008).

Selective attenuation and decoupled propagation methods can be extended to viscoelastic media and 3D. However, a limitation is that both are built on the assumption of decoupled elastic wavefields, which means they are only valid for isotropic elastic media. Vector decomposition for VTI media is also possible by solving the Christoffel equation (Zhang and McMechan, 2010) at significantly greater expense. Cheaper and more accurate vector decomposition methods for anisotropic media need to be explored.

A fundamental reason for doing the vector wavefield-decomposition is the potential for application in elastic RTM. In this paper, we implement and illustrate methods to decompose the elastic x-z wavefields during extrapolation, and to decompose x-t seismograms into P and S components. This will lead to two different strategies of implementing elastic RTMs: We can either use the original elastic seismograms as input and decompose the wavefields during extrapolation, or we can use the decomposed P and S seismograms directly as input for elastic RTMs. Selective attenuation can potentially be used with viscoelastic migration, in which one wave mode is removed by attenuation and the other is compensated for by viscoelastic losses in the same extrapolation. These, and the corresponding PP and PS imaging conditions, will be presented elsewhere.

CONCLUSIONS

Vector decomposition of P- and S-waves is superior to the traditional divergence and curl separation because the latter damage the amplitude and phase of the input elastic wavefields. Because wavefield vector decomposition preserves all elastic vector information, the amplitude and phase remain accurate after decomposition. Two affordable methods for isotropic elastic decomposition in the vector domain (selective attenuation and decoupled propagation) are implemented, illustrated, and compared. Both are performed during extrapolation. Synthetic tests show that both methods give accurate decomposition results for homogeneous and smoothly varying isotropic models. The decoupled propagation is better in terms of accuracy, speed, memory requirement, and numerical stability. Decomposition of the observed x-t data into P and S vector seismograms can be achieved by downward, followed by upward, elastic wavefield extrapolations through a homogeneous model with either of the wavefield-decomposition algorithms and reconstruction of the decomposed seismograms.

ACKNOWLEDGMENTS

The research leading to this paper is supported by the sponsors of the UT-Dallas Geophysical Consortium. A portion of the computations was done at the Texas Advanced Computing Center. This paper is contribution no. 1270 from the Department of Geosciences at the University of Texas at Dallas. Special thanks go to J. Brown, A. Shabelansky, and two anonymous reviewers for their useful comments and encouragements.

APPENDIX A

PROOF OF EQUIVALENCE OF TWO DECOUPLED ELASTIC PROPAGATION ALGORITHMS

Zhang et al. (2007) propose an algorithm for decomposition of an elastic wavefield, which is a decoupled version of Virieux's (1986) staggered-grid stress-velocity formulation. In that algorithm, the P and S particle velocities are solved simultaneously. Xiao and Leaney (1986) use an additional variable σ_P to construct the decoupled elastic equation, which is more efficient and intuitive. The two algorithms can be proved to be mathematically equivalent as follows.

We start with a 2D version of the Xiao and Leaney (2010) decomposition algorithm, in which Virieux's (1986) stress-particle velocity equations are completely preserved. Refer to equations 14–23.

If we add the equations 14 and 15, we obtain

$$\frac{\partial \sigma_{xx}}{\partial t}+\frac{\partial \sigma_{zz}}{\partial t}=(2\lambda+2\mu)\left(\frac{\partial v_x}{\partial x}+\frac{\partial v_z}{\partial z}\right). \tag{A-1}$$

Replacing $\frac{\partial v_x}{\partial x}+\frac{\partial v_z}{\partial z}$ with $\frac{1}{\lambda+2\mu}\frac{\partial \sigma_P}{\partial t}$, from equation 19 into equation A-2, we get

$$\frac{\partial \sigma_{xx}}{\partial t}+\frac{\partial \sigma_{zz}}{\partial t}=\frac{2\lambda+2\mu}{\lambda+2\mu}\frac{\partial \sigma_P}{\partial t}. \tag{A-2}$$

Substituting for $\frac{\partial \sigma_P}{\partial t}$ from equation A-2 into equations 20 and 21, the time derivatives of the P-wave x and z particle-velocity components become

$$\frac{\partial v_{x\mathrm{P}}}{\partial t}=\frac{1}{\rho}\frac{\lambda+2\mu}{2\lambda+2\mu}\left(\frac{\partial \sigma_{xx}}{\partial x}+\frac{\partial \sigma_{zz}}{\partial x}\right), \tag{A-3}$$

and

$$\frac{\partial v_{z\mathrm{P}}}{\partial t}=\frac{1}{\rho}\frac{\lambda+2\mu}{2\lambda+2\mu}\left(\frac{\partial \sigma_{xx}}{\partial z}+\frac{\partial \sigma_{zz}}{\partial z}\right). \tag{A-4}$$

With the expressions v_i (where i is x or z) and $v_{i\mathrm{P}}$, the subtraction form of $v_{i\mathrm{S}}$ in equations 22 and 23 can be rewritten as

$$\begin{aligned}\frac{\partial v_{x\mathrm{S}}}{\partial t}&=\frac{\partial v_x}{\partial t}-\frac{\partial v_{x\mathrm{P}}}{\partial t}\\&=\frac{1}{\rho}\frac{\lambda}{2\lambda+2\mu}\frac{\partial \sigma_{xx}}{\partial x}+\frac{1}{\rho}\frac{\partial \sigma_{xz}}{\partial z}-\frac{1}{\rho}\frac{\lambda+2\mu}{2\lambda+2\mu}\frac{\partial \sigma_{zz}}{\partial x}\end{aligned} \tag{A-5}$$

and

$$\begin{aligned}\frac{\partial v_{z\mathrm{S}}}{\partial t}&=\frac{\partial v_z}{\partial t}-\frac{\partial v_{z\mathrm{P}}}{\partial t}\\&=\frac{1}{\rho}\frac{\lambda}{2\lambda+2\mu}\frac{\partial \sigma_{zz}}{\partial z}+\frac{1}{\rho}\frac{\partial \sigma_{xz}}{\partial x}-\frac{1}{\rho}\frac{\lambda+2\mu}{2\lambda+2\mu}\frac{\partial \sigma_{xx}}{\partial z}.\end{aligned} \tag{A-6}$$

The sum of $v_{i\mathrm{S}}$ and $v_{i\mathrm{P}}$ forms the complete particle-velocity component description of the S and P parts of the elastic wavefield. Thus,

$$v_x=v_{x\mathrm{S}}+v_{x\mathrm{P}} \tag{A-7}$$

and

$$v_z=v_{z\mathrm{S}}+v_{z\mathrm{P}}, \tag{A-8}$$

which are equations 22 and 23. Equations A-3–A-8 form the algorithm of Zhang et al. (2007) Q.E.D.

REFERENCES

Aki, K., and P. G. Richards, 1980, Quantitative seismology, theory and methods: W. H. Freeman and Co.

Bourbie, T., O. Coussy, and B. Zinzner, 1987, Acoustic of porous media: Gulf Publishing Company.

Carcione, J. M., 1993, Seismic modeling in viscoelastic media: Geophysics, **58**, 110–120, doi: 10.1190/1.1443340.

Carcione, J. M., D. Kosloff, and R. Kosloff, 1988a, Wave propagation in a linear viscoelastic medium: Geophysical Journal, **95**, 597–611, doi: 10.1111/j.1365-246X.1988.tb06706.x.

Carcione, J. M., D. Kosloff, and R. Kosloff, 1988b, Viscoacoustic wave propagation simulation in the earth: Geophysics, **53**, 769–777, doi: 10.1190/1.1442512.

Chattopadhyay, S., and G. A. McMechan, 2008, Imaging conditions for prestack reverse time migration: Geophysics, **73**, no. 3, S81–S89, doi: 10.1190/1.2903822.

Cheng, J., and S. Fomel, 2014, Fast algorithms for elastic-wave-mode separation and vector decomposition using low-rank approximation for anisotropic media: Geophysics, **79**, no. 4, C97–C110, doi: 10.1190/geo2014-0032.1.

Clayton, R. W., 1981, Wavefield inversion methods for refraction and reflection data: Ph.D. thesis, Stanford University.

Dablain, M. A., 1986, The application of high-order differencing to the scalar wave equation: Geophysics, **51**, 54–66, doi: 10.1190/1.1442040.

Dellinger, J., and J. Etgen, 1990, Wave-field separation in two-dimensional anisotropic media: Geophysics, **55**, 914–919, doi: 10.1190/1.1442906.

Emmerich, H., and M. Korn, 1987, Incorporation of attenuation into time-domain computations of seismic wave fields: Geophysics, **52**, 1252–1264, doi: 10.1190/1.1442386.

Guéguen, Y., and V. Palciauskas, 1994, Introduction to the physics of rocks: Princeton University Press.

Komatitsch, D., and R. Martin, 2007, An unsplit convolutional perfectly matched layer improved at grazing incidence for the seismic wave equation: Geophysics, **72**, no. 5, SM155–SM167, doi: 10.1190/1.2757586.

Levander, A. R., 1988, Fourth-order finite-difference P-SV seismograms: Geophysics, **53**, 1425–1436, doi: 10.1190/1.1442422.

Liu, R., D. L. Anderson, and H. Kanamori, 1976, Velocity dispersion due to anelasticity: Implication for seismology and mantle composition: Geophysical Journal of the Royal Astronomical Society, **47**, 41–58, doi: 10.1111/j.1365-246X.1976.tb01261.x.

Ma, D., and G. Zhu, 2003, P- and S-wave separated elastic wave equation numerical modeling (in Chinese): Oil Geophysical Prospecting, **38**, 482–486, doi: 10.1190/1.1442147.

McDonal, F. J., F. A. Angona, R. L. Mills, R. L. Sengbush, R. G. van Nostrand, and J. E. White, 1958, Attenuation of shear and compressional waves in Pierre shale: Geophysics, **23**, 421–439, doi: 10.1190/1.1438489.

Mora, P., 1987, Nonlinear two-dimensional elastic inversion of multioffset seismic data: Geophysics, **52**, 1211–1228, doi: 10.1190/1.1442384.

Morse, P. M., and H. Feshbach, 1953, Methods of theoretical physics: McGraw-Hill Book Company.

Nguyen, B. D., and G. A. McMechan, 2015, Five ways to avoid storing source wavefield snapshots in 2D elastic prestack reverse-time migration: Geophysics, **80**, no. 1 S1–S18, doi: 10.1190/geo2014-0014.1.

Robertsson, J. O., J. O. Blanch, and W. W. Symes, 1994, Viscoelastic finite-difference modeling: Geophysics, **59**, 1444–1456, doi: 10.1190/1.1443701.

Sun, R., 1999, Separating P- and S-waves in a prestack 2-dimensional elastic seismogram: 61st Annual International Conference and Exhibition, EAGE, Extended Abstracts, 6–23.

Sun, R., J. Chow, and K. J. Chen, 2001, Phase correction in separating P- and S-waves in elastic data: Geophysics, **66**, 1515–1518, doi: 10.1190/1.1487097.

Sun, R., and G. A. McMechan, 2001, Scalar reverse-time depth migration of prestack elastic seismic data: Geophysics, **66**, 1518–1527, doi: 10.1190/1.1487098.

Sun, R., G. A. McMechan, and H. Chuang, 2011, Amplitude balancing in separating P- and S-waves in 2D and 3D elastic seismic data: Geophysics, **76**, no. 3, S103–S113, doi: 10.1190/1.3555529.

Virieux, J., 1986, P-SV wave propagation in heterogeneous media — Velocity-stress finite difference method: Geophysics, **51**, 889–901, doi: 10.1190/1.1442147.

Xiao, X., and W. S. Leaney, 2010, Local vertical seismic profiling (VSP) elastic reverse-time migration and migration resolution — Salt-flank imaging with transmitted P-to-S waves: Geophysics, **75**, no. 2, S35–S49, doi: 10.1190/1.3309460.

Xu, T., and G. A. McMechan, 1995, Composite memory variables for viscoelastic synthetic seismograms: Geophysical Journal International, **121**, 634–639, doi: 10.1111/j.1365-246X.1995.tb05738.x.

Yan, J., and P. Sava, 2008, Elastic wavefield separation for VTI media: 78th Annual International Meeting, SEG, Expanded Abstracts, 2191–2195.

Zener, C., 1948, Elasticity and anelasticity of metals: University of Chicago Press.

Zhang, J., Z. Tian, and C. Wang, 2007, P- and S-wave separated elastic wave equation numerical modeling using 2D staggered-grid: 77th Annual International Meeting, SEG, Expanded Abstracts, 2104–2109.

Zhang, Q., and G. A. McMechan, 2010, 2D and 3D elastic wavefield vector decomposition in the wavenumber domain for VTI media: Geophysics, **75**, no. 3, D13–D26, doi: 10.1190/1.3431045.